
SUPPLEMENTAL MATERIALS

1 MODEL ARCHITECTURE

The detailed architecture of our generator is shown on Table 1.

Layers	Output Size	Generator
Linear	(128, 4, 4)	Linear 128×2048
Upsampling	(128, 8, 8)	Upsampling 2×2
SPADE ResBlk-1	(128, 8, 8)	SPADE 128, Leaky ReLU Convolution 3×3 SPADE 128, Leaky ReLU Convolution 3×3
Upsampling	(128, 16, 16)	Upsampling 2×2
SPADE ResBlk-2	(128, 16, 16)	SPADE 128, Leaky ReLU Convolution 3×3 SPADE 128, Leaky ReLU Convolution 3×3
Upsampling	(128, 32, 32)	Upsampling 2×2
SPADE ResBlk-3	(64, 32, 32)	SPADE 128, Leaky ReLU Convolution 3×3 SPADE 64, Leaky ReLU Convolution 3×3 SPADE 64, Leaky ReLU Shortcut Convolution 3×3
Upsampling	(64, 64, 64)	Upsampling 2×2
SPADE ResBlk-4	(64, 64, 64)	SPADE 64, Leaky ReLU Convolution 3×3 SPADE 64, Leaky ReLU Convolution 3×3
Convolution	(24, 64, 64)	Leaky ReLU, Convolution 5×5
Convolution	(24 * 8, 64, 64)	Leaky ReLU, Convolution 5×5
Group SPADE	(24 * 8, 64, 64)	[SPADE 8] * 24
Modulation	(24 * 64, 64, 64) (24, 64, 64)	[Outer Product $8 \otimes 8$] * 24 Convolution 1×1 , Sigmoid
Output	(24, 64, 64)	Sum residual, Sigmoid

Table 1: Architecture details of CCIGAN’s generator

where ResBlk is the residual block with skip connection used in ResNet (He et al., 2016), and SPADE is the spatially-adaptive normalization layer. The detailed architecture of our discriminator is shown on Table 2.

Layers	Output Size	Discriminator
Conv-1	(32, 32, 32)	Convolution 4×4 , stride 2 Instance Norm, Leaky ReLU
Conv-2	(64, 16, 16)	Convolution 4×4 , stride 2 Instance Norm, Leaky ReLU
Conv-3	(128, 8, 8)	Convolution 4×4 , stride 2 Instance Norm, Leaky ReLU
Conv-4	(256, 4, 4)	Convolution 4×4 , stride 2 Instance Norm, Leaky ReLU
Conv-5	(512, 2, 2)	Convolution 4×4 , stride 2 Instance Norm, Leaky ReLU
Conv-6	(1, 1, 1)	Convolution 3×3 , stride 2 Sigmoid

Table 2: Architecture details of CCIGAN’s discriminator

1.1 IMPLEMENTATION DETAILS AND TRAINING REGIMEN

Our implementation of the generator applies Spectral Norm to all layers (Miyato et al., 2018). The discriminator’s input is the output of the generator concatenated with the segmentation patch $[\mathbf{X}, \mathbf{S}]$ and $[\mathbf{Y}, \mathbf{S}]$ for the ground truth. Finally CCIGAN uses ADAM ($lr_G = 0.0004$, $lr_D = 0.0001$) with GAN loss and feature matching loss. Full training details and loss functions are as follows.

1.2 MODEL TRAINING

G is the generator and D is the discriminator for CCIGAN. Given segmentation map \mathbf{S} , ground truth \mathbf{Y} and noise δ , the generated image is $\mathbf{X} = G(\mathbf{S}, \delta)$. The input of the discriminator is the cell image conditioned on the segmentation map \mathbf{S} . We use LSGAN loss (Mao et al., 2017) in CCIGAN, which is defined as follows:

$$L_{GAN}(G, D) = \mathbb{E}_{\mathbf{Y}, \mathbf{S}} [\|D(\mathbf{Y}, \mathbf{S})\|_2] + \mathbb{E}_{\mathbf{S}} [\|1 - D(G(\mathbf{S}, \delta), \mathbf{S})\|_2] \quad (1)$$

In addition to GAN loss, we also use feature matching loss (Wang et al., 2018) during training expressed as:

$$L_{FM}(G, D) = \mathbb{E}_{\mathbf{Y}, \mathbf{S}} \sum_{j=1}^J \frac{1}{N_j} [\|D_j(\mathbf{Y}, \mathbf{S}) - D_j(G(\mathbf{S}, \delta), \mathbf{S})\|_1] \quad (2)$$

where D_j is j -th layer feature map of the discriminator for $j \in \{1, \dots, J\}$, and N_j is the number of elements in j -th layer. Consequently, the objective function for training is given as follows:

$$\min_G \left(\left(\max_D L_{GAN}(G, D) \right) + \lambda L_{FM}(G, D) \right) \quad (3)$$

where $\lambda = 10$. Due to the size of cell patch is $(64, 64)$, we do not use multi-scale discriminators and perceptual loss in CCIGAN and other baseline models e.g. SPADE and pix2pixHD.

In training, we use ADAM as the optimizer. The generator learning rate is $lr_G = 0.0004$ and the discriminator learning rate is $lr_D = 0.0001$. We train CCIGAN 120 epochs with a training set of 5648 cell patches. We train other baseline models for 120 epochs or until they converge (max 150). The full details of training of CCIGAN and baselines are shown as Table 3. The hyperparameters of each model are fine-tuned to get better performance. The training time was roughly equal for all models. In particular, CCIGAN was around 1.2 times slower than the SPADE baseline on a single Tesla V100 GPU.

Metrics	Ours	SPADE	Pix2PixHD	CycleGAN
lr_G	0.0004	0.0008	0.0002	0.0002
lr_D	0.0001	0.0001	0.0002	0.0002

Table 3: Hyperparameters of models

1.3 MODEL INTERPRETABILITY AND GENERATIVENESS

Examining the model's persistent vectors s_m , we can try to understand if there is a match between real world protein markers and the representations of s_m . For example, the vector s_{pk} for pan-keratin attends to tumor cells and s_{CD8} attends to CD8 T cells at pixel pairwise levels. It follows that in a simple experiment where corresponding $s_{CD8} \leftrightarrow s_{pk}$ vectors are exchanged internally in the attention module (Eq. 10, Figure 1 (Step 3) of Main Paper , outer product) we may observe a lower expression for tumor cells in channel m_{pk} and a lower expression for CD8 T cells in channel m_{CD8} since tumor cells do not express CD8 and CD8 T cells do not express pan-keratin. As a control, we also switch surface membrane markers HLA Class 1 and dsDNA markers as they are present in all cells and have very similar average expression values ($s_{HLAcl} \leftrightarrow s_{dsDNA}$). Accordingly, for our control, we expect to see negligible changes. We define the expression ratio as $\frac{\text{after}}{\text{before}} - 1$.

Protein Markers	CD8	pan keratin	HLA Class 1	dsDNA
Expression Ratios	-0.373	-0.145	-0.054	-0.0012

Table 4: s_m persistent vector interpretability experiments.

In Table 10, we can see a larger magnitude decrease of the expression ratios in the $s_{CD8} \leftrightarrow s_{pk}$ experiment and a minute difference in the $s_{HLAcl} \leftrightarrow s_{dsDNA}$. Further visualizations (Figure 1) and discussion (model generativeness, Figure 2) are as follows.

Figure 1 shows the persistent vectors s_i for all proteins. Note the similarity between CD3 and CD8 T cell protein markers and the similarity between dsDNA and HLA Class 1 surface membrane proteins (expressed in all cells). It is also important to make the distinction that sparse markers (while different) are similar in state. This is due to the lack of training data for rare cell types, making it difficult for the model to reason on such a small sample size.

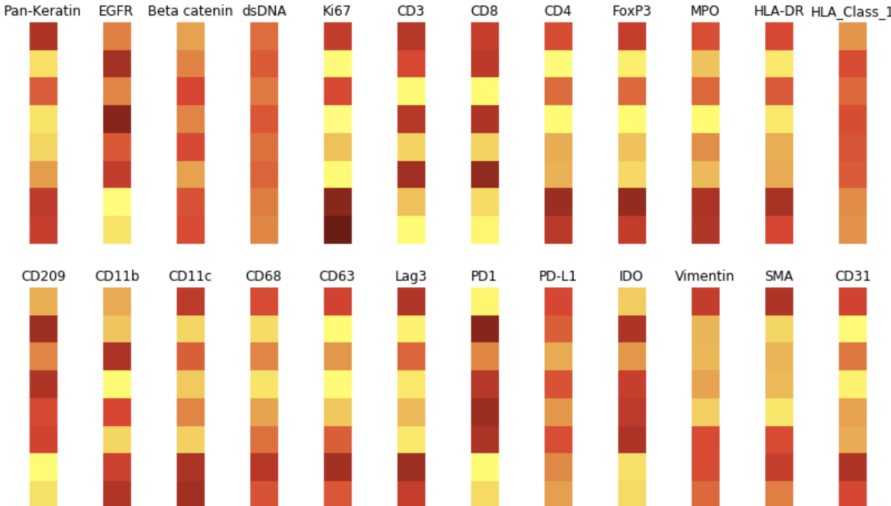


Figure 1: Persistent vectors s for various channels.

Figure 2 shows the generativeness of CCIGAN through an uncertainty map over 100 instances (random noise). An uncertainty map shows the differences per pixel (x, y) location. The higher intensities indicate a higher probability of changing at the specified (x, y) location.

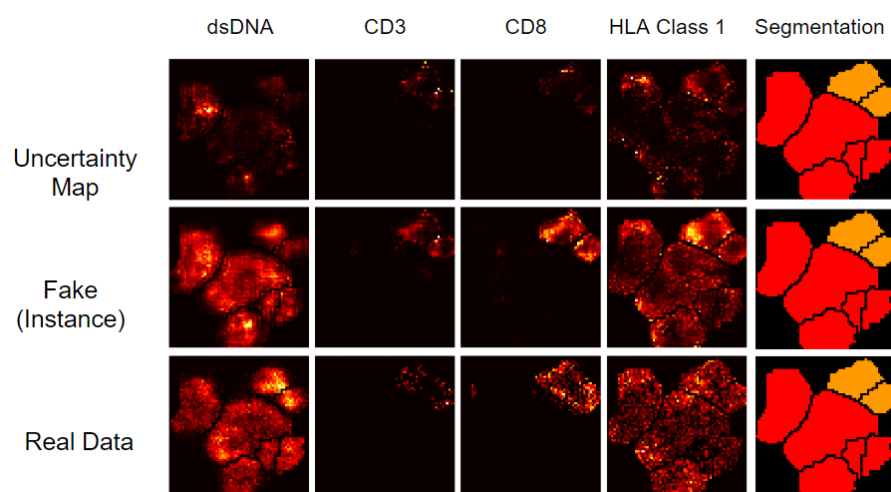


Figure 2: Uncertainty maps illustrating model generativeness.

2 DATA AND DATA PROCESSING

2.1 MIBI-TOF

Multiplexed ion beam imaging by time-of-flight (MIBI-TOF) represents a novel technology that can accurately quantify and spatially resolve cellular protein expressions at the single cell level within tissue samples. Given a tissue sample that is first stained with protein-specific antibodies tethered to elemental metals, MIBI-TOF bombards the sample with atomic ions (i.e. O_2^+) from a primary ion beam. This causes the release of elemental isotopes and tissue-specific material which can be quantified in a mass spectrometer (Angelo et al., 2014).

For MIBI, the markers used (total 24) in our experiments are: Pan-Keratin, EGFR, Beta catenin, dsDNA, Ki67, CD3, CD8, CD4, FoxP3, MPO, HLA-DR, HLA-Class-1, CD209, CD11b, CD11c, CD68, CD63, Lag3, PD1, PD-L1, IODO, Vimentin, SMA, CD31. The markers we didn't use (total 12) in our experiments are: CD16, B7H3, CD45, CD45RO, Keratin17, CD20, CD163, CD56, Keratin6, CSF-1R, p53, CD138. These were not used primarily due to blank expressions.

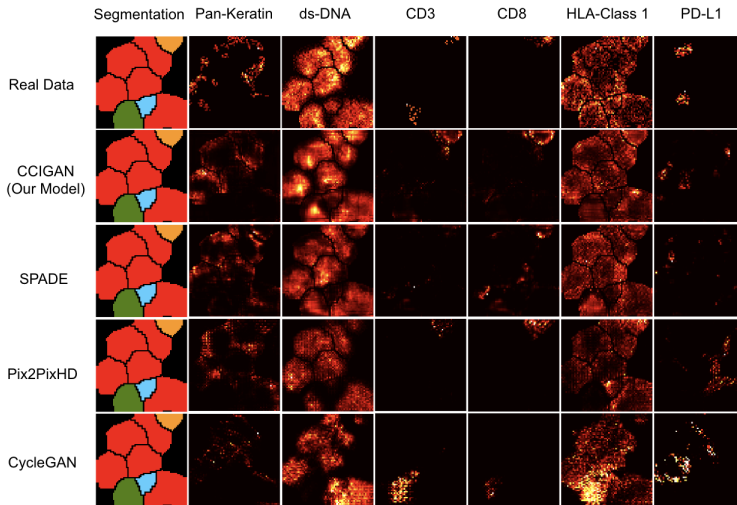


Figure 3: Examples generated from a segmentation for certain channels for different models. The segmentation patch is the one hot encoded patch collapsed and colored into 1 channel. The horizontal labels represent protein markers and the vertical labels are each of the generative models.

2.2 t-CyCIF

The t-CyCIF images are obtained through iterative cycles of incubating the sample with antibodies (markers) conjugated directly with fluorophores that will bind to a specific protein of interest, imaging the samples with a microscope to record the light emitted at each location of the protein, then deactivating the fluorescence signal by soaking the sample in a compound (Rashid et al., 2019) . At each iteration, different antibodies that bind to different proteins of interests are applied. After obtaining multiple images with few channels at each iteration, the images are stitched together to produce a high-dimension image.

For t-CyCIF, the markers used (total 37) are: DAPI1, DAPI2, DAPI3, LAG3, ARL13B, DAPI4, KI67, KERATIN, PD1, DAPI5, CD45RB, CD3D, PDL1, DAPI6, CD4, CD45, CD8A, DAPI7, CD163, CD68, CD14, DAPI8, CD11B, FOXP3, CD21, DAPI9, IBA1, ASMA, CD20, DAPI10, CD19, GFAP, GTUBULIN, DAPI11, LAMINAC, BANF1, LAMINB. The markers we didn't use (total 7) are: A488background1, A555background1, A647background1, A488background2, A555background2, A647background2, A488background3.

2.2.1 T-CyCIF DATA PREPROCESSING

For t-CyCIF data, each cell was first clustered to one of many cell types. Using cell features (log cell expression data), we clustered the cells using the 26 non-DAPI markers. We exponentiated the cell features data to restore the data to raw cell intensities, then quantile clipped each marker to retain only the data from 1% to 99.5%. After 0-1 min-max rescaling the data, we clustered the cells using the Phenograph tool, developed in the Dana Pe'er Lab (Levine et al., 2015).

Let N denote the nuclear probability matrix of the image where $N_{i,j} = \Pr[\text{nucleus at index } (i,j)]$ and let N' be the 0-1 nuclear segmentation mask, $N'_{i,j} = \mathbb{1}[\text{cell nucleus at index } (i,j)]$. Cytoplasm probabilities were also provided, the cytoplasm probability mask is denoted as C , where $C_{i,j} = \Pr[\text{cytoplasm at index } (i,j)]$. N, N', C were provided to us from Rashid et al. (2019). We modified the cytoplasm probability mask to a 0-1 cytoplasm mask C' where $C'_{i,j} = \mathbb{1}[C_{i,j} > 0.4 \wedge N_{i,j} < 0.4]$ by choosing these thresholds ourselves. Then we overlayed the nuclear and cytoplasm masks together to form a mask T of the total cell, where $T_{i,j} = \mathbb{1}[\text{a cell occurs at index } (i,j)]$. Because there are small holes in this mask, we filled the holes using SK-image's morphology tools. To yield the final segmentation mask F , we dilated the nuclear segmentation mask N' with 2 iterations and perform an element-wise mask with mask T , where $F_{i,j} = \mathbb{1}[N'_{i,j} = 1 \wedge T_{i,j} = 1]$.

2.2.2 T-CYCIF DATA SPLIT

We split the t-CyCIF primary lung cancer dataset into four segments to test our hypothesis that CCIGAN can learn biological relationships specific to tumor microenvironments with varying characteristics. Three segments (highly, semi, and poorly infiltrated) were each manually selected based on the visible proportion of lymphocyte presence within the tumor microenvironment. Figures 4 and 5 show the segments in relation to the lymphocyte and keratin expression. More detailed descriptions of each individual dataset segment are as follows.

T_1 Infiltrated - High proportion of lymphocyte presence within the tumor microenvironment. Indicative of a strong inflammatory anti-tumor immune response.

T_2 Semi-infiltrated - Medium levels of lymphocyte infiltration within the tumor microenvironment.

T_3 Poorly-infiltrated - Few lymphocytes present within the tumor microenvironment indicative of a poor anti-tumor immune response.

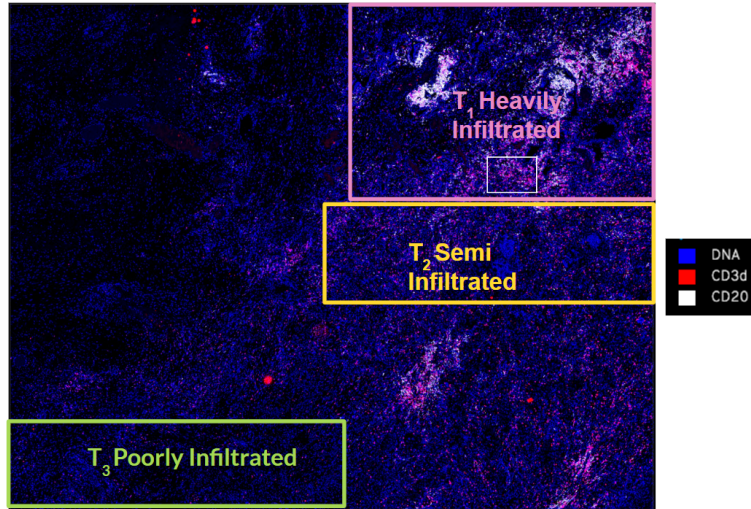


Figure 4: Splits of the tissue with lymphocyte cell protein markers highlighted

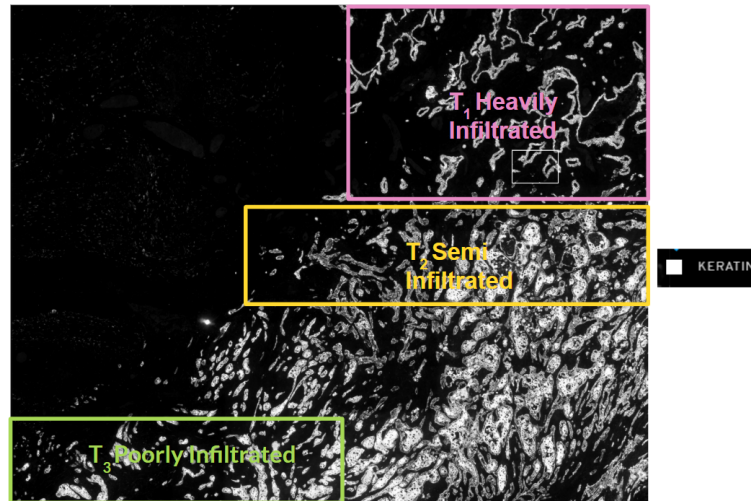


Figure 5: Splits of the tissue with keratin positive tumor cell type highlighted

2.3 DATA LIMITATIONS

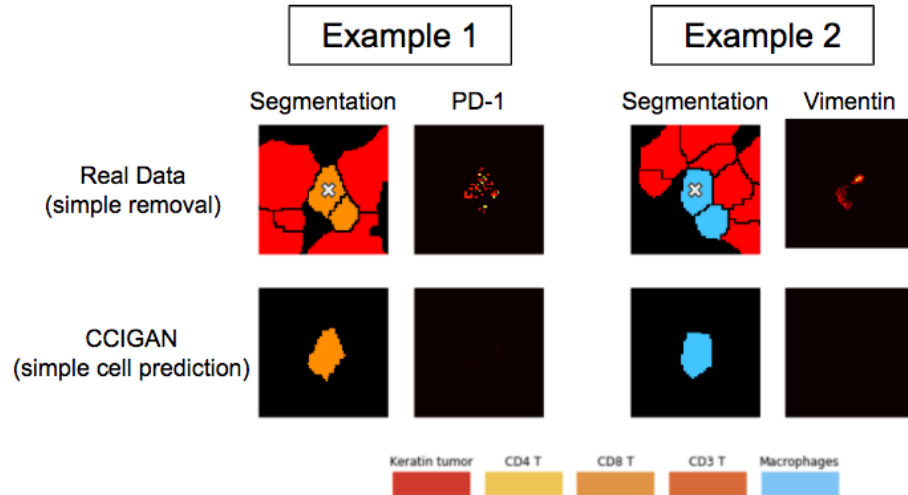


Figure 6: Data limitations regarding manually isolating cells and their protein localizations. Simply deleting cells surrounding a target cell does not reveal the true protein localization of the target cell (with the X marker), as the protein localization will still assume a neighboring interactions. In Example 1, the target CD8 T cell should only express PD-1 when it is surrounded by PD-L1 expressing tumor cells which upregulate the PD-1 expression. Note in the real data how deleting the surrounding cells do not change its PD-1 protein localization. CCIGAN learns that for an isolated CD8 T cell, PD-1 is not upregulated and therefore not expressed.

3 EVALUATION

3.1 CENTER OF MASS (COM)

Figure 7 shows an illustration of the center of mass and projected center of mass of a patch of tumor and CD8 T cells.

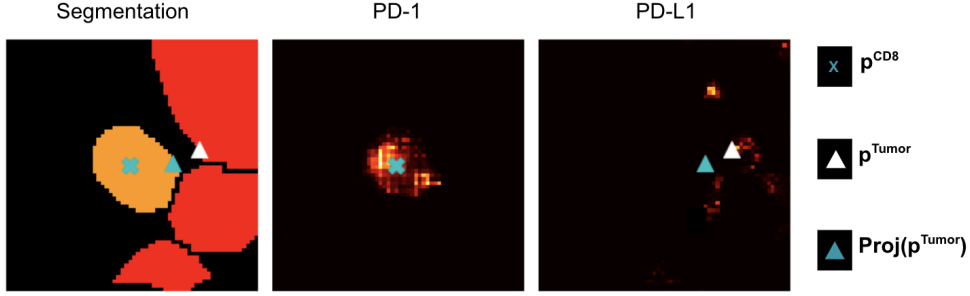


Figure 7: An example illustration of the center of mass (COM) nomenclature from section 3.1. Note the projection onto the CD8 T cell. This provides a more consistent measurement across different patches by projecting p^{Tumor} onto the CD8 T cell.

3.2 EARTH MOVER'S DISTANCE

Figures 8 and 9 demonstrate the directional and histogram shifts as a function of adding more tumor cells.

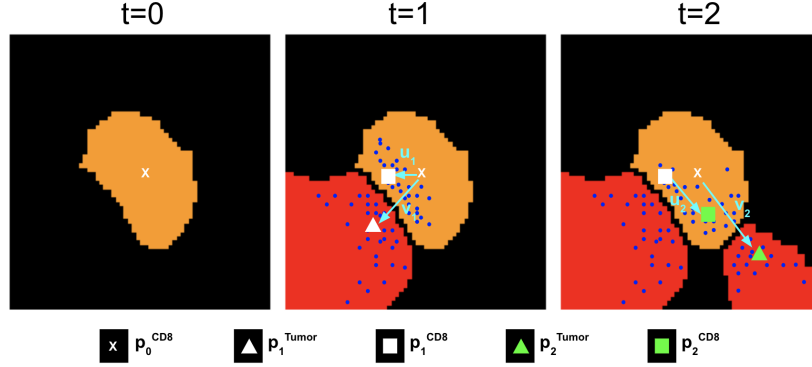


Figure 8: An example illustration of the points and vector nomenclature from section 5.2. The blue dots are the expression of PD-1 and PD-L1 proteins. The cyan arrows show the vectors v_t and u_t . Note the shift in expression of the PD-1 as a response to the added tumor's PD-L1 expression.

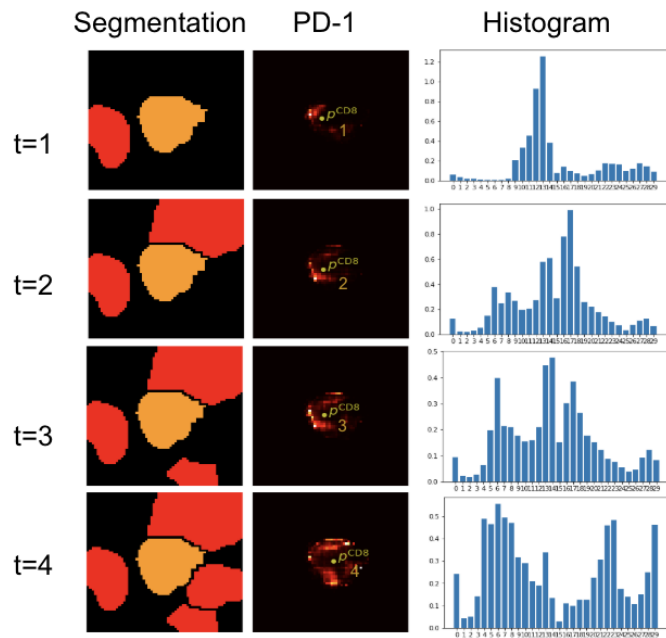


Figure 9: Example illustration of how a CD8 T cell's (orange) PD-1 histogram changes as a function of iteratively added tumor cells.

3.3 RECONSTRUCTION METRICS

Given the generated image set $\mathcal{X} = \{\mathbf{X}_i\}_{i=1}^N$ and the ground truth set $\mathcal{Y} = \{\mathbf{Y}_i\}_{i=1}^N$ with $\mathbf{X}_i, \mathbf{Y}_i \in \mathbb{R}^{(M,H,W)}$, the L_1/MSE score is defined as follows,

$$L(\mathcal{X}, \mathcal{Y}) = \sum_{i=1}^N \sum_{m=1}^M \|\text{sort}(\mathbf{U}_i \odot \mathbf{X}_{i,m}) - \text{sort}(\mathbf{U}_i \odot \mathbf{Y}_{i,m})\|_* \quad (4)$$

where $\|\cdot\|_*$ can be either L_1 or L_2 norm, \odot is the element-wise product, $\mathbf{X}_{i,m}$ and $\mathbf{Y}_{i,m}$ are the m -th channel of the i -th cell patch, $\mathbf{U}_i \in \{0, 1\}^{(H,W)}$ is the mask matrix which masks all the cells in i -th patch. For any matrix \mathbf{A} , $\text{sort}(\mathbf{A})$ is the sort function that sorts all entries of \mathbf{A} . The sorting function ensures our metrics are position independent and only measures the intensity of the generated image and ground truth. The score function $L(\mathcal{X}, \mathcal{Y})$ only computes the loss of sorted expression inside of the cells. Then we add penalization for expression outside of cells. The adjusted L_1/MSE score is introduced as follows,

$$\begin{aligned} L_{\text{adj}}(\mathcal{X}, \mathcal{Y}) = & \sum_{m=1}^M \left(\|\text{sort}(\mathbf{U}_i \odot \mathbf{X}_{i,m}) - \text{sort}(\mathbf{U}_i \odot \mathbf{Y}_{i,m})\| \right. \\ & \left. - \|\text{sort}((\mathbf{1}_d - \mathbf{U}_i) \odot \mathbf{X}_{i,m}) - \text{sort}((\mathbf{1}_d - \mathbf{U}_i) \odot \mathbf{Y}_{i,m})\| \right) \end{aligned} \quad (5)$$

where $\mathbf{1}_d$ is the matrix with all entries equal to 1. A smaller score indicates a better result.

For any two images $\mathbf{X}, \mathbf{Y} \in [0, 1]^{(H,W)}$, the SSIM and MI are defined as:

$$\text{SSIM}(\mathbf{X}, \mathbf{Y}) = \frac{(2\mu_X\mu_Y + c_1)(2\sigma_{XY} + c_2)}{(\mu_X^2 + \mu_Y^2 + c_1)(\sigma_X^2 + \sigma_Y^2 + c_2)} \quad (6) \quad I(\mathbf{X}; \mathbf{Y}) = H(\mathbf{X}) + H(\mathbf{Y}) - H(\mathbf{X}, \mathbf{Y}) \quad (7)$$

where $H(\cdot)$ is entropy, μ_X and σ_X are the mean and standard deviation of \mathbf{X} , c_1, c_2 are constants. Then the SSIM between \mathcal{X}, \mathcal{Y} is

$$\text{SSIM}(\mathcal{X}, \mathcal{Y}) = \frac{1}{N} \frac{1}{M} \sum_{i=1}^N \sum_{m=1}^M \text{SSIM}(\mathbf{X}_{i,m}, \mathbf{Y}_{i,m}) \quad (8)$$

In cell based MI, test patches are processed at a cell-cell basis where their mutual information is computed with the corresponding cell in the ground truth. For the generated image \mathbf{X}_i of the i -th patch, we assume there are T_i cells in the i -th patch. Then for each cell t , the pixels of m -th channel of the t -th cell in the i -th patch can be expressed as a vector $\mathbf{x}_{i,m}^t$. Hence, the cell based MI is formulated as:

$$I(\mathcal{X}; \mathcal{Y}) = \frac{1}{\sum_{i=1}^N T_i} \frac{1}{M} \sum_{i=1}^N \sum_{m=1}^M \left(\sum_{t=1}^{T_i} I(\mathbf{x}_{i,m}^t; \mathbf{y}_{i,m}^t) \right) \quad (9)$$

The SSIM measures the similarity between the generated image and the ground truth. For SSIM, we use HLA Class 1 and dsDNA due to their expressions in all cells. If all channels were considered, the SSIM would be uninformative due to the majority of the channels being blank or sparse. The MI measures the information shared between generated image and ground truth at a cell by cell basis where we consider all channels. Consider the example where a model generates no expression in marker m but the real data has expression in m , the MI would be 0 and vice versa. Higher SSIM and MI values indicate better results.

3.4 PAN-KERATIN AND CD8 EXPRESSION

The pan-keratin/CD8 experiment is similar to Figure 17's orientation except the center cell (cell of interest) is a tumor cell (red) and the adjacent neighboring cells are CD8 T cells (orange). CCIGAN predicted a decrease in tumor cell pan-keratin expression with respect to increasing CD8 T cell area/number (Figure 10). This is juxtaposed to the tumor cell control where there is no change in the pan-keratin level as the number of neighboring tumor cells is increased.

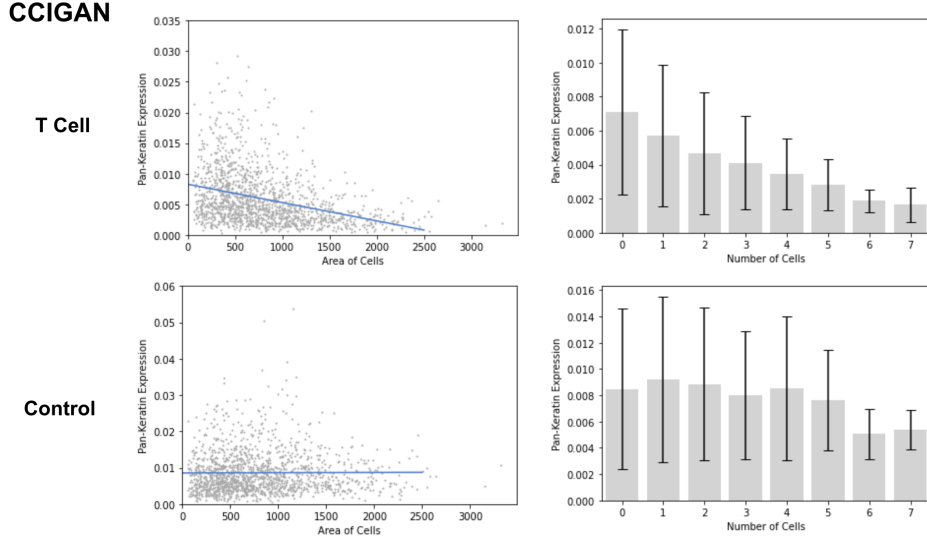


Figure 10: CCIGAN experiment for adding CD8 T cells and tumor cells (control) around a tumor cell.

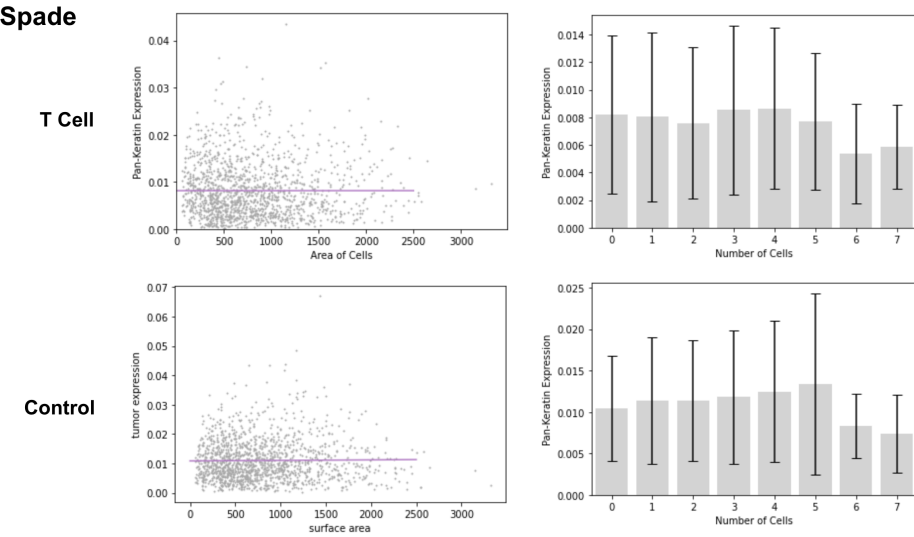


Figure 11: SPADE experiment for adding CD8 T cells and tumor cells (control) around a tumor cell.

SPADE does not predict a decrease in tumor cell pan-keratin expression with respect to increasing CD8 T cell area/number and shows no difference in pan-keratin expression trends between the T

cell and control groups (Figure 11).

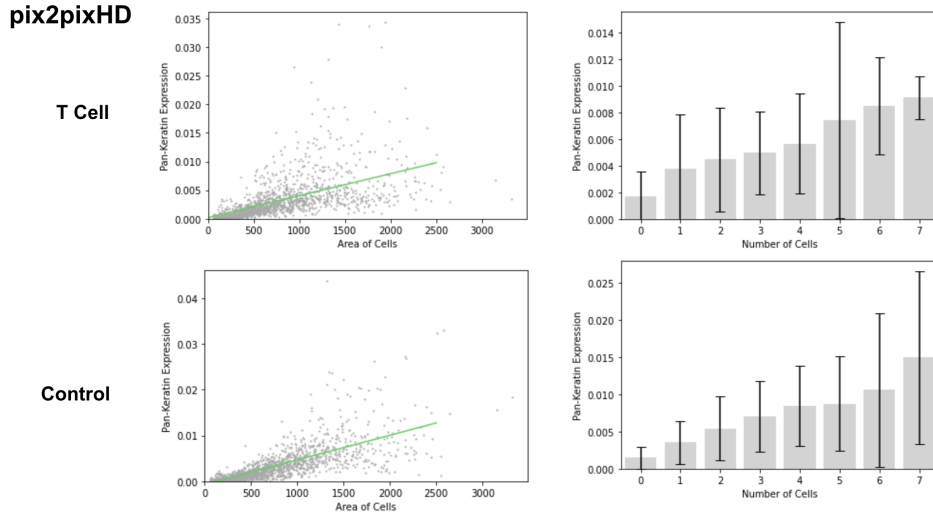


Figure 12: pix2pixHD experiment for adding CD8 T cells and tumor cells (control) around a tumor cell.

pix2pixHD erroneously predicts an increase in tumor cell pan-keratin expression with respect to increasing CD8 T cell area/number and shows no difference in pan-keratin expression trends between the T cell and control groups (Figure 12).

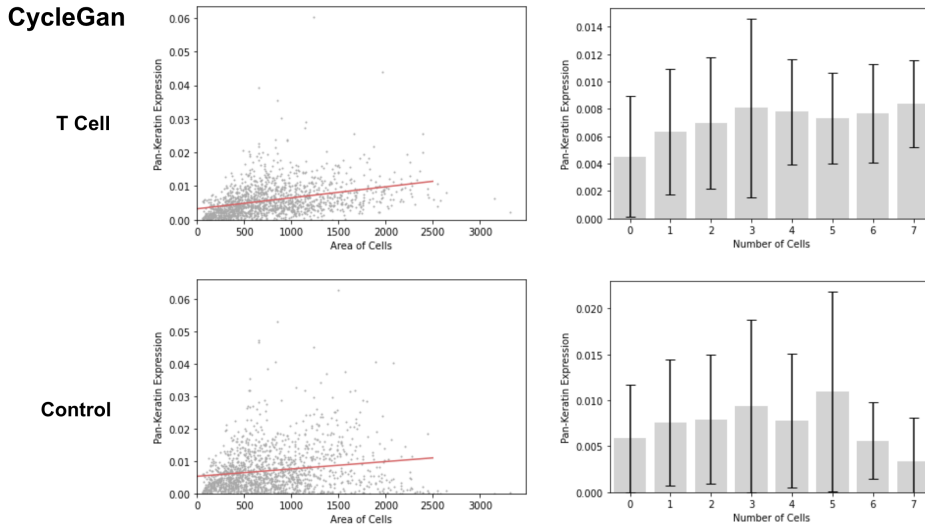


Figure 13: CycleGAN experiment for adding CD8 T cells and tumor cells (control) around a tumor cell.

CycleGAN fails to predict a decrease in tumor cell pan-keratin expression with respect to increasing CD8 T cell area/number and shows no difference in pan-keratin expression trends between the T cell and control groups (Figure 13).

3.5 TUMOR INFILTRATED AND COMPARTMENTALIZED MICROENVIRONMENTS

Keren et al. (2018) determined that in situations of mixed tumor-immune environments, where immune cells freely infiltrated the tumor, the tumor cells predominantly expressed PD-L1. Conversely, in situations of compartmentalized tumors, where there is a greater degree of physical separation between immune and tumor cells, macrophages were the predominant source of expressed PD-L1, particularly at the tumor boundary.

These findings were recapitulated by CCIGAN. For a patient with a mixed tumor environment, when trained with mixed patient samples, CCIGAN reported increased PD-L1 expression on tumor cells. Furthermore, CCIGAN was able to quantify this difference in expression at the single cell level, reporting a tumor to macrophage PD-L1 expression ratio of approximately 3.2 and 1.75 for patients A and B respectively.

Conversely, when trained with compartmentalized patient samples, CCIGAN reported increased PD-L1 expression on macrophages adjacent to tumor cells when compared to macrophages adjacent to normal endothelial (inert) cells. This difference was quantified as a ratio of PD-L1 expression of tumor-adjacent macrophages to endothelial-adjacent macrophages, approximately 1.85 and 2.7 for patient C and patient D respectively.

Below are tables of the data used to generate figure 3D of the main paper. Results from testing increased PD-1/PD-L1 expression from the bolded cell being challenged with another cell type in its microenvironment are located in table 5. The 3rd column shows summed pixel intensity of the specified protein expression.

In table 6, the second row shows that even when using the trained compartmentalized model to predict on mixed segmentation patches, CCIGAN still reports a 26% (patient C) and 19% (patient D) increase of macrophage PD-L1 expression when compared to mixed microenvironments (Table 6).

Experiment	Microenvironments	Patient A	Patient B
PD-1 (T cell)	T cell / Tumor / Macrophages	0.01886	0.00131
	T cell / Endothelial / Macrophages	0.00558	0.00107
PD-L1 (Tumor)	T cell / Tumor / Macrophages	0.00649	0.00100
	Endothelial / Tumor / Macrophages	0.00279	0.00046
PD-L1 (Macrophages)	T cell / Tumor / Macrophages	0.00204	0.00057
	T cell / Endothelial / Macrophages	0.00068	0.00047

Table 5: Average PD-1/PD-L1 expression on the mixed tumor environment. The bolded cells indicate which cells are being measured.

Experiment (Macrophages)	Microenvironments	Patient C	Patient D
PD-L1 (Compartmentalized)	T cell / Tumor / Macrophages	0.00408	0.00608
	T cell / Endothelial / Macrophages	0.00220	0.00225
PD-L1 (Mixed)	T cell / Tumor / Macrophages	0.00324	0.00510

Table 6: Average PDL1 expression of macrophages/monocytes on the compartmentalized tumor environment.

Environment	T_1	T_2	T_3
Slope	2.629×10^{-3}	2.953×10^{-3}	3.134×10^{-3}
t-test	36.715	14.341	23.803
p-value	3.079×10^{-225}	1.945×10^{-44}	2.848×10^{-110}

Table 7: Slope and statistical values for t-CyCIF PD-1/PD-L1 Trend Experiment with respect to surrounding tumor cell surface area.

3.6 T-CYCIF PD-1/PD-L1 TREND EXPERIMENT (FIGURE 3F) EXPLANATIONS

By training CCIGAN models on different segments of the t-CyCIF dataset (2.2.2), we investigate the relationship between PD-1 and PD-L1. Using the same experimental setting as 3.4, our cell of interest (center cell) is a CD8 T cell and we iteratively add tumor cells as adjacent neighboring cells. Figure 18 shows an example patch of a CD8 T cell (orange) in the center and iteratively adding tumor cells (yellow). As surrounding tumor cell surface area increases and surrounding PD-L1 expression increases, we expect PD-1 in the CD8 T cell to be upregulated, as it is an indicator of T cell exhaustion. PD-1 expression trend differs depending on the level of tumor-infiltration in the tumor microenvironment. In a poorly infiltrated microenvironment, the PD-1 expression trend should be greater than in a highly infiltrated microenvironment, since low infiltration indicates greater immunosuppression and a higher rate of T cell exhaustion. Our results as shown in main paper Figure 3F are fully displayed in Figure 14, which illustrates sample runs, and table 7, which shows the full trend and statistical values from Figure 3F. Additionally, we plotted the slope trend of CD8 T cell PD-1 expression against surrounding total tumor PD-L1 expression in table 8

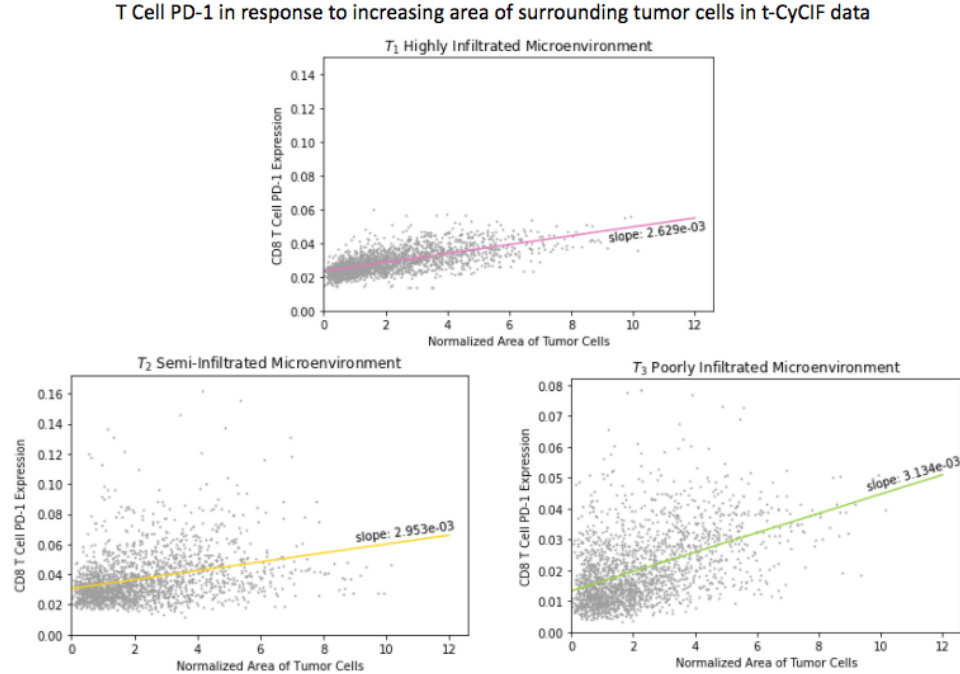


Figure 14: PD-1/PD-L1 experiment on tumor microenvironments with varying levels of tumor-infiltration in t-CyCIF (3.6) with respect to surrounding tumor cell surface area.

Environment	T_1	T_2	T_3
Slope	4.339×10^{-5}	5.450×10^{-5}	2.970×10^{-4}
<i>t</i> -test	35.248	14.477	25.608
<i>p</i> -value	2.098×10^{-211}	3.285×10^{-45}	4.520×10^{-125}

Table 8: Slope and statistical values for t-CyCIF PD-1/PD-L1 Trend Experiment with respect to total surrounding PD-L1 expression.

T Cell PD-1 in response to increasing PD-L1 expressing tumor cells in t-CyCIF data

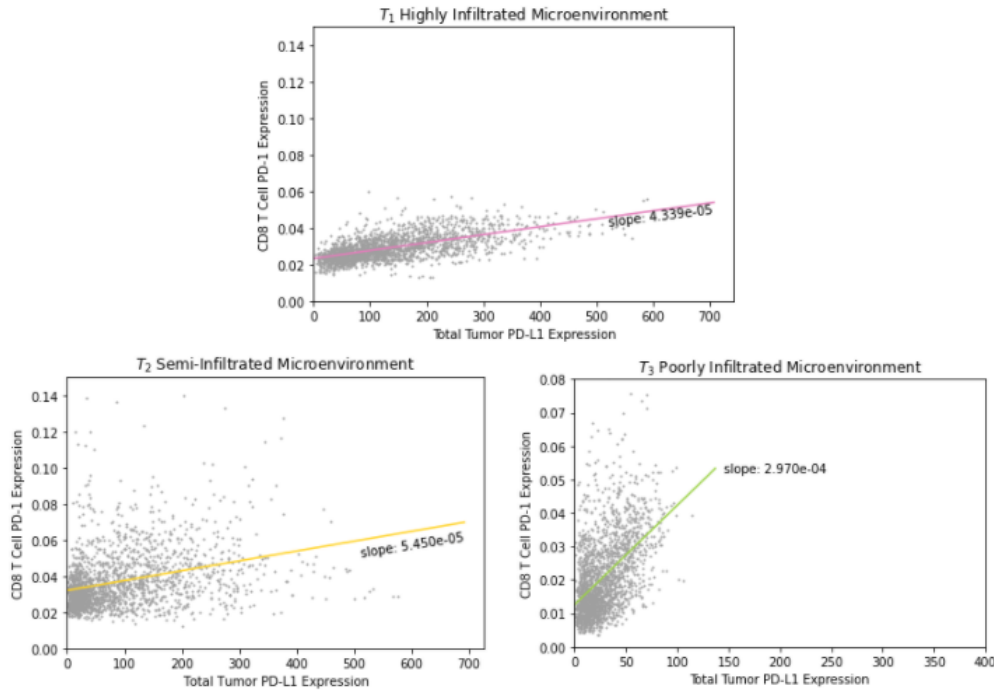


Figure 15: PD-1/PD-L1 experiment on tumor microenvironments with varying levels of tumor-infiltration in t-CyCIF (3.6) with respect to total surrounding PD-L1 expression.

Environment	T_1	T_2	T_3
Slope	4.843×10^{-5}	8.838×10^{-5}	6.242×10^{-4}
<i>t</i> -test	35.778	12.711	21.693
<i>p</i> -value	2.172×10^{-216}	1.238×10^{-35}	9.723×10^{-94}

Table 9: Slope and statistical values for t-CyCIF LAG3/PD-L1 Trend Experiment.

3.7 T-CYCIF LAG3/PD-L1 TREND EXPERIMENT (FIGURE 3G) EXPLANATIONS

Furthermore, we investigate the relationship between LAG3 and PD-L1. Using the same experimental setting as 3.5, our cell of interest (center cell) is a CD8 T cell and the adjacent neighboring cells are tumor cells. As tumor cells are added and the surrounding PD-L1 expression increases, we expect LAG3 in the CD8 T cell to be upregulated, as it is another indicator of T cell exhaustion. Similarly to 3.5, we expect a higher trend of LAG3 upregulation with respect to PD-L1 in microenvironments with lower tumor-infiltration. Our results as shown in main paper Figure 3G are fully displayed in Figure 16, which illustrates sample runs, and table 9, which shows the full trend and statistical values from Figure 3F.

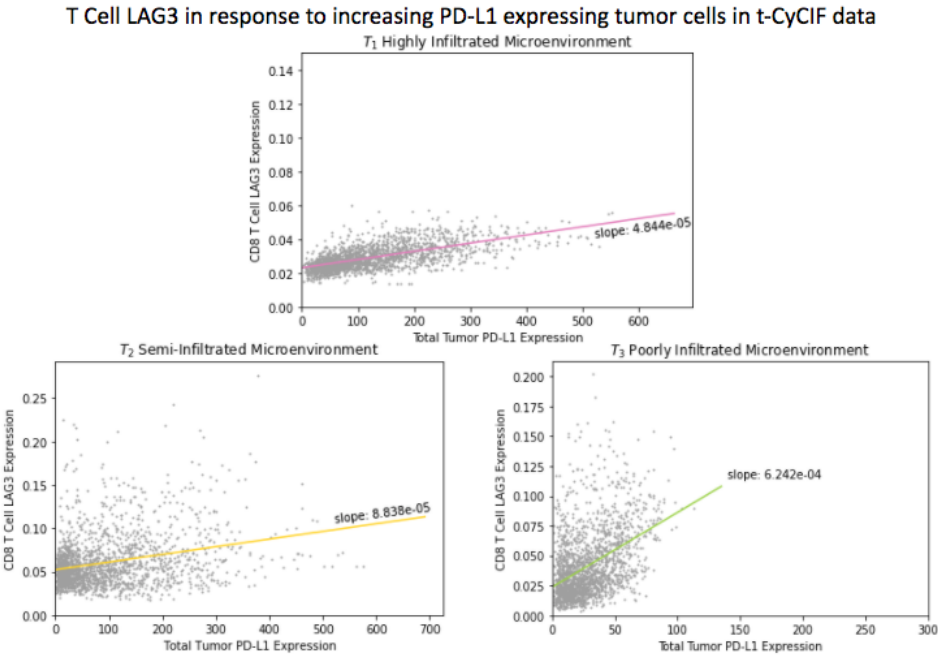


Figure 16: LAG3/PD-1 experiment on tumor microenvironments with varying levels of tumor-infiltration in t-CyCIF

4 FURTHER EXPERIMENTS AND EXPERIMENT DETAILS

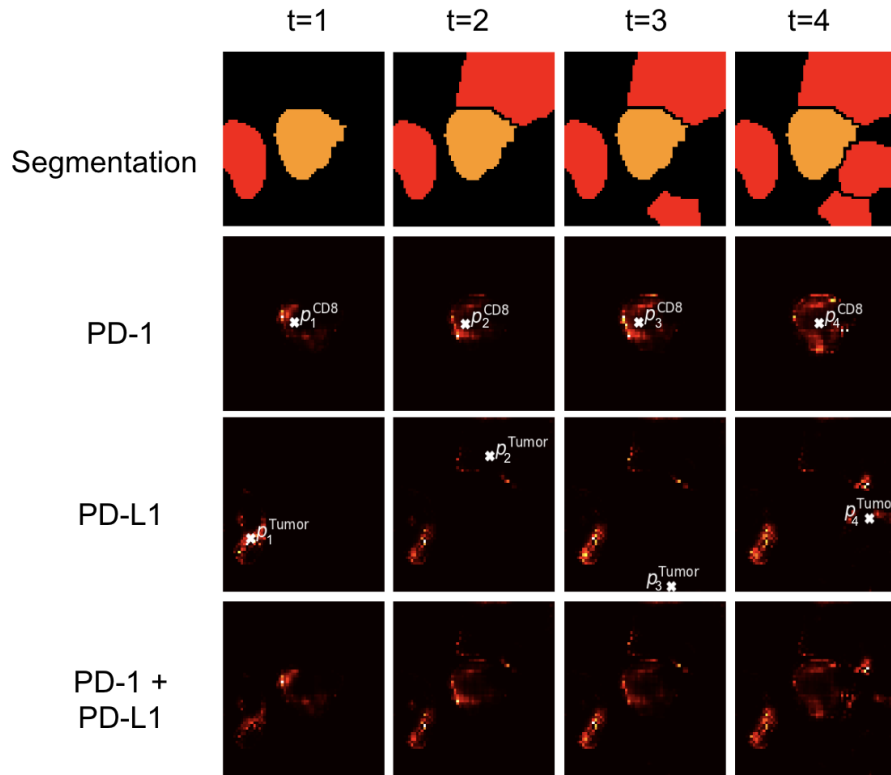


Figure 17: Process of iteratively adding tumor cells in MIBI-TOF. The added red cells are tumor cells (PD-L1) and the center orange cell indicates a CD8 T cell (cell of interest, PD-1). For this process, we focus on each instance of an added tumor.

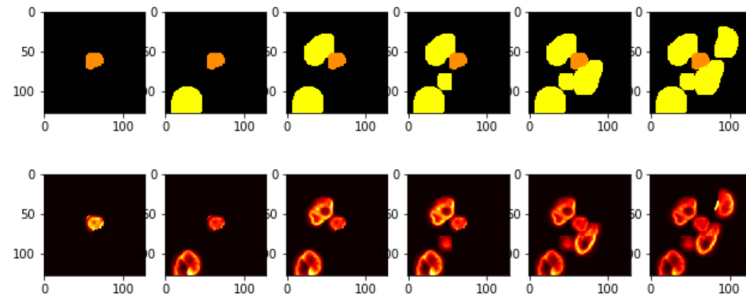


Figure 18: Iteratively Adding Cells for t-CyCIF data. A random dsDNA protein channel is shown.

4.1 EXPERIMENTAL SETUP

In our general experiments that involved iteratively manipulating cell patches, we created a experimental dataset of approximately 1000 patches for each type of data (MIBI-TOF or t-CyCIF) and manipulated the cell types to the necessary cell types for each experiment. For a patch s in the experimental dataset with n cells in the patch, we expanded the patch into n individual patches $P_s = \{p_1^{(s)}, p_2^{(s)}, \dots, p_n^{(s)}\}$ where for $0 \leq i \leq n$, $p_i^{(s)}$ = patch of cells from 1 to i . An example can be seen in Figure 17 for MIBI data where PD-1 expression in the CD 8 T cell of interest reacts to newly introduced PD-L1 expressing tumor cells. Another example is shown for t-CyCIF data in Figure 18. Following this, changes in protein expressions in the cell of interest due to newly introduced cells were analyzed using a variety of techniques (center of mass, summation, mass shift, regression trend).

4.2 FIGURE 4E DISCUSSION

In this section we discuss potential biological trends, erroneous correlations, and algorithm settings. It is important to note that some of the spurious correlations are easily explained by poor segmentations (known issue).

Figure 3E displays the results of our search algorithm, which shows which particular cell-cell interactions are significantly captured in CCIGAN. For four primary cells– tumor, macrophage, CD8, and endothelial, we measure their expression level change in a subset of protein markers and calculate the relative frequency of this cell-cell interaction. Using a subset of 1268 test cell patches, we counted the number of significant logged interactions that produced an increase or decrease in expression level greater than a chosen threshold. Expression level change was measured by simply calculating the difference in summed pixel intensity (protein expression) in a particular channel.

For the relative frequency of a particular cell-cell interaction, the normalization schema is as follows. Using the logged counts of significant changes in expression level, we take the max of either the increase counts or the decrease counts. Then, to quantify the ratio of relative importance within a primary cell group, we divide the max counts by the total number of logged counts (for either only increases or decreases). For example, say we are measuring tumor as the primary cell. If 100 decreases and 200 increases in expression level are recorded, with 1000 total increases logged for the tumor primary cell, $200/1000 = 0.2$ is the relative frequency after normalization.

1. Vimentin

It was observed that nearly all scenarios of cell-cell interaction accounted for by CCIGAN resulted in an varying increases of vimentin expression in the cell of interest. While not necessarily biologically explained, the observed changes are plausible as vimentin is a structural protein found in all cells and changes in its levels may not be attributable to specific cell interactions. A continued investigation is given in 4.2.1 regarding tumor and CD 8 T cell vimentin expressions.

2. PD-1

A slight increase in the PD-1 expression is seen on tumor cells when surrounded by CD8 T cells. However, this increase was negligible and can be attributed to noisy segmentations where PD-1 expressing CD8 T cells are located near tumor cells, suggesting in the training data that a tumor cell expresses PD-1.

3. PD-L1

The model suggests PD-L1 expression on CD8 T cells despite this not being true. This is due to noisy segmentations similar to the situation in PD-1.

4. CD8

The model predicted an increase in CD8 expression on the tumor cell in several scenarios despite this not being biologically expected. This also due to the same noisy segmentations.

5. Pan Keratin

The decreased levels in Pan Keratin expression within the tumor cell line with neighboring non-tumor cells was biologically expected. However, the slight increase in pan keratin expression when the tumor cell of interest had tumor cell neighbors may be due to the same noisy segmentations as mentioned before.

Algorithm settings were set on the same sensitivity threshold for experiments. Additionally, figure generation normalization was done across protein markers (within different cell groups). Finally, interactions comprising of 5% or less of total logged interactions were disregarded.

4.2.1 VIMENTIN TABLE EXPRESSIONS

As a continuation from exploration 3E, we measure trends of vimentin expression in tumor cells due to varying amounts of surrounding CD 8 T cells. The cell of interest is a tumor cell and we iteratively change surrounding adjacent cells from tumor cells to CD8 T cells with different probabilities. Then we measure the number of instances a change of vimentin is detected, and what that change is.

Cell of Interest	Adjacent Cell Neighbor %	% of Patches Indicating Increase in Vimentin
Tumor	100% CD8 0% Tumor	91.6%
Tumor	75% CD8 25% Tumor	81.6%
Tumor	50% CD8 50% Tumor	60.4%
Tumor	25% CD8 75% Tumor	26.7%

Table 10: Table indicating net changes in Vimentin expression in a tumor cells due to increasing CD8 T cell presence.

REFERENCES

- S. C. Angelo, M. and Bendall, R. Finck, M. B. Hale, C. Hitzman, A. D. Borowsky, R. M. Levenson, J. B. Lowe, S. D. Liu, S. Zhao, Y. Natkunam, and G. P. Nolan. Multiplexed ion beam imaging of human breast tumors. *Nature Medicine*, 20:436–442, 2014.
- Kaiming He, Xiangyu Zhang, Shaoqing Ren, and Jian Sun. Deep residual learning for image recognition. In *Proceedings of the IEEE conference on computer vision and pattern recognition*, pp. 770–778, 2016.
- Jacob H. Levine, Erin F. Simonds, Sean C. Bendall, Kara L. Davis, Elad D. Amir, Michelle D. Tadmor, Oren Litvin, Harris G. Fienberg, Astraea Jager, Eli R. Zunder, Rachel Finck, Amanda L. Gedman, Ina Radtke, James R. Downing, Dana Pe'er, and Garry P. Nolan. Data-driven phenotypic dissection of AML reveals progenitor-like cells that correlate with prognosis. *Cell*, 162(1):184–197, jul 2015. doi: 10.1016/j.cell.2015.05.047. URL <http://dx.doi.org/10.1016/j.cell.2015.05.047>.
- Xudong Mao, Qing Li, Haoran Xie, Raymond YK Lau, Zhen Wang, and Stephen Paul Smolley. Least squares generative adversarial networks. In *Proceedings of the IEEE International Conference on Computer Vision*, pp. 2794–2802, 2017.
- Takeru Miyato, Toshiki Kataoka, Masanori Koyama, and Yuichi Yoshida. Spectral normalization for generative adversarial networks. *CoRR*, abs/1802.05957, 2018. URL <http://arxiv.org/abs/1802.05957>.
- Rumana Rashid, Giorgio Gaglia, Yu-An Chen, Jia-Ren Lin, Ziming Du, Zoltan Maliga, Denis Schapiro, Clarence Yapp, Jeremy Muhlich, Artem Sokolov, Peter Sorger, and Sandro Santagata. Highly multiplexed immunofluorescence images and single-cell data of immune markers in tonsil and lung cancer. *bioRxiv*, 2019. doi: 10.1101/704114. URL <https://www.biorxiv.org/content/early/2019/07/17/704114>.
- Ting-Chun Wang, Ming-Yu Liu, Jun-Yan Zhu, Andrew Tao, Jan Kautz, and Bryan Catanzaro. High-resolution image synthesis and semantic manipulation with conditional gans. In *Proceedings of the IEEE Conference on Computer Vision and Pattern Recognition*, 2018.